A precise photometric ratio via laser excitation of the sodium layer - I. One-photon excitation using 342.78 nm light

Justin E. Albert, Dmitry Budker, Kelly Chance, Iouli E. Gordon, Felipe Pedreros Bustos, Maxim Pospelov, Simon M. Rochester, H. R. Sadeghpour

Monthly Notices
of the
ROYAL ASTRONOMICAL SOCIETY

MNRAS **508,** 4399–4411 (2021)
Advance Access publication 2021 June 7

https://doi.org/10.1093/mnras/stab1621

A precise photometric ratio via laser excitation of the sodium layer – I. One-photon excitation using 342.78 nm light

Justin E. Albert [1]★ Dmitry Budker [2,3,4] Kelly Chance [5] Iouli E. Gordon [5]
Felipe Pedreros Bustos [2,6] Maxim Pospelov,[1,7,8] Simon M. Rochester [4] and H. R. Sadeghpour [3]

[1]*Department of Physics and Astronomy, University of Victoria, Victoria, British Columbia V8W 3P6, Canada*
[2]*Helmholtz Institute, Johannes Gutenberg-Universität Mainz, D-55099 Mainz, Germany*
[3]*Rochester Scientific LLC, El Cerrito, CA 94530, USA*
[4]*Department of Physics, University of California, Berkeley, CA 94720-7300, USA*
[5]*Harvard-Smithsonian Center for Astrophysics, Cambridge, MA 02138, USA*
[6]*Laboratoire d'Astrophysique de Marseille (LAM), Université d'Aix-Marseille & CNRS, F-13388 Marseille, France*
[7]*Perimeter Institute of Theoretical Physics, Waterloo, Ontario N2L 2Y5, Canada*
[8]*Now at School of Physics and Astronomy, University of Minnesota, Minneapolis, MN 55455, USA*

Accepted 2021 June 3. Received 2021 June 3; in original form 2021 January 18

ABSTRACT

The largest uncertainty on measurements of dark energy using type Ia supernovae (SNeIa) is presently due to systematics from photometry; specifically to the relative uncertainty on photometry as a function of wavelength in the optical spectrum. We show that a precise constraint on relative photometry between the visible and near-infrared can be achieved at upcoming survey telescopes, such as at the Vera C. Rubin Observatory, via a laser source tuned to the 342.78 nm vacuum excitation wavelength of neutral sodium atoms. Using a high-power laser, this excitation will produce an artificial star, which we term a 'laser photometric ratio star' (LPRS) of de-excitation light in the mesosphere at wavelengths in vacuum of 589.16, 589.76, 818.55, and 819.70 nm, with the sum of the numbers of 589.16 and 589.76 nm photons produced by this process equal to the sum of the numbers of 818.55 and 819.70 nm photons, establishing a precise calibration ratio between, for example, the *r* and *z* filters of the LSST camera at the Rubin Observatory. This technique can thus provide a novel mechanism for establishing a spectrophotometric calibration ratio of unprecedented precision for upcoming telescopic observations across astronomy and atmospheric physics; thus greatly improving the performance of upcoming measurements of dark energy parameters using type SNeIa. The second paper of this pair describes an alternative technique to achieve a similar, but brighter, LPRS than the technique described in this paper, by using two lasers near resonances at 589.16 and 819.71 nm, rather than the single 342.78 nm on-resonance laser technique described in this paper.

Key words: techniques: photometric – methods: observational – telescopes – instrumentation: miscellaneous – dark energy.

1 MOTIVATIONS

Over two-thirds of the total mass-energy of the Universe is dark energy, a mysterious characteristic of space with measured properties that are consistent, at present, with being those of the cosmological constant from the field equations of general relativity (Lahav & Liddle 2019; Aghanim et al. 2020). The value of the cosmological constant, and its possible relation to the zero-point energies of quantum fields is, however, a notoriously longstanding problem at the intersection of quantum mechanics and general relativity that predates the discovery, two decades ago, of non-zero dark energy (Riess et al. 1998; Perlmutter et al. 1999) by several additional decades (Weinberg 1989). The large uncertainties at present on multiple parameters of dark energy, especially on any changes that dark energy may have undergone over cosmic history, ensure that the improvement in measurement of dark energy properties remains at the forefront of observational cosmology and astrophysics.

Measurements of dark energy utilizing the method of its discovery, i.e. the construction of a Hubble curve with type Ia supernovae (SNeIa) have, for the past 10 years or so, been limited primarily by systematic uncertainty on the measurement of astronomical magnitude as a function of colour within the optical spectrum (Wood-Vasey et al. 2007; Betoule et al. 2014). The statistics of observed SNeIa have continued to improve (Jones et al. 2018), and will improve dramatically with the beginning of the Vera C. Rubin Observatory sky survey (known as the 'Legacy Survey of Space and Time,' or LSST) in the early 2020s (Ivezić et al. 2019). The systematic limitation from spectrophotometry will continue, however, to be a fundamental barrier to major improvement on measurements in this area (Stubbs & Tonry 2006).

Beyond dark energy measurements with SNeIa, the precision of relative spectrophotometry also is presently a limiting factor in measurements of stellar populations in galaxy clusters (Connor et al. 2017) and in upcoming photometric redshift surveys measuring growth of structure (Kirk et al. 2015).

★ E-mail: jalbert@uvic.ca

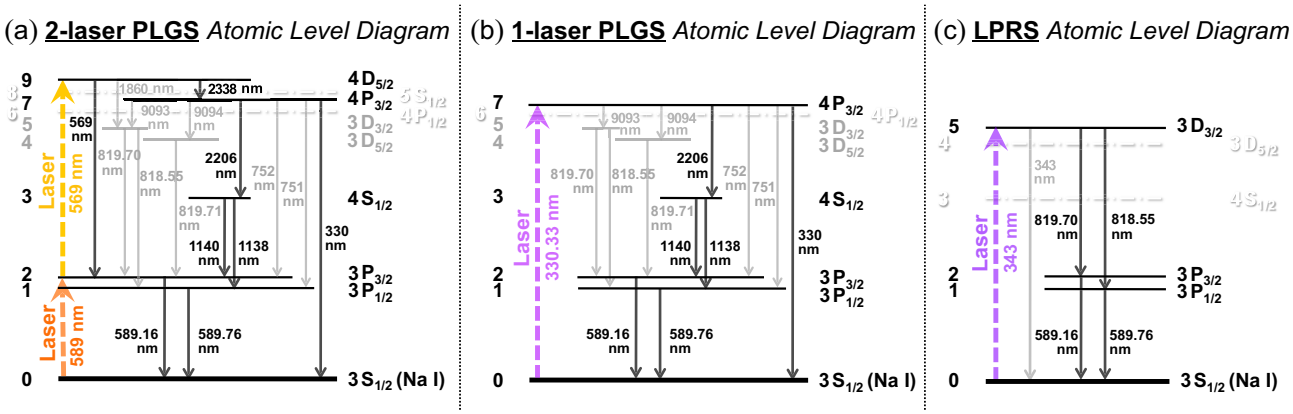

Figure 1. Atomic level diagrams for neutral sodium atoms (not to scale): (a) for two-laser polychromatic laser guide stars (PLGS), (b) for one-laser PLGS, and (c) for a laser photometric ratio star (LPRS). 'Forbidden' magnetic dipole and electric quadrupole transitions, and also the levels (and decays from the levels) that are only accessible by such transitions, are in solid grey, whereas allowed and laser-excited transitions and levels are in solid black. 'Ghost' levels, which are entirely inaccessible from states in the diagrams that are excited by the lasers, are shown in shadowed grey text and dash–dotted lines. As can be seen, the relatively simple LPRS diagram results in 'fully-mandated cascades' from the 819/820 nm de-excitations to the 589/590 nm de-excitations, resulting in a mandated 1:1 ratio between those produced photons, whereas the cascades in the relatively more complex PLGS diagrams do not have such absolutely mandated ratios between their produced photons of different wavelengths. (The simplicity of the LPRS diagram is counterbalanced by the weakness of the 343 nm transition when compared with the transitions excited by PLGS lasers, which results in LPRS being much dimmer than PLGS.)

2 EXISTING RELATED INFRASTRUCTURE AND THE ATMOSPHERIC SODIUM LAYER

Within the separate astronomical domain of point-spread function (PSF) minimization and calibration, laser guide stars (LGS) have dramatically improved the angular resolution of ground-based telescopic imaging and spectroscopy over the past decades, within the fields of view of major deep-field observatories employing LGS and adaptive optics (AO) (Olivier & Max 1994; Bonaccini et al. 2002; Wizinowich et al. 2006). LGS produce resonant scattering of light from the layer of atomic sodium in the Earth's mesosphere by utilizing lasers located at observatory sites and typically tuned to the sodium D_2-line resonance at 589 nm.

The Earth's atmospheric layer of neutral atomic sodium (Na I) (Slipher 1929) exists between approximately 80 and 105 km above sea level. It originates primarily from the ablation of meteors in the ionosphere (Chapman 1939; Plane, Feng & Dawkins 2015); with a potentially significant fraction of upper-atmospheric Na I atoms having instead been (somewhat surprisingly) previously located on the regolith of the Moon, ejected from the Moon's surface by meteoritic impacts, swept into a long lunar Na I tail that is pointed away from the Sun, and then intercepted by the Earth during new moon periods (Potter & Morgan 1988a,b; Baumgardner et al. 2021). The Earth's total atmospheric column density of sodium varies with time and location between about 2×10^9 atoms cm^{-2} and 8×10^9 atoms cm^{-2} (Mégie et al. 1978; Moussaoui et al. 2010). Current LGS typically use a solid-state laser or a fiber laser,[1] with typical optical output power around 10 – 20W, directed into the mesosphere to produce an artificial star at about 9^{th} magnitude,[2] which is sufficient for real-time deformable mirror AO image correction at 4-m class and larger observatories.

Sodium is not especially abundant in comparison to other atomic and molecular species in the upper atmosphere, but the product of its density and its optical cross-section [with Einstein A coefficients of 6.16×10^7 s^{-1} and 6.14×10^7 s^{-1} (Juncar et al. 1981; Kramida et al. 2020) for the Na 589.16 and 589.76 nm resonances[3] respectively] makes sodium the most favourable element for optical excitation.[4] Due to the poorly-predictable variability of the Na column density (as well as other trace elemental column densities), LGS do not have major utility for precise calibration of photometry, but rather find their utility, as mentioned above, in minimization and calibration of PSF, when combined with AO.

Polychromatic LGS (PLGS), which produce artificial stars with one or more optical wavelengths in addition to either one or both of the sodium D lines, were first conceived by Foy et al. (1995) and have since been tested on the sky (Foy et al. 2000), but not yet utilized within a full closed AO loop. PLGS have a significant advantage over monochromatic LGS (MLGS) in that PLGS can, in principle, provide the information necessary to compensate first-order atmospheric aberrations ('tip-tilt') based on differential measurements of the tip-tilt at two separated wavelengths (Foy & Pique 2004; Tyson 2015), whereas MLGS lack this capability (necessitating the simultaneous use of a sufficiently-bright natural guide star, which has a low probability of existing in close vicinity to the object of interest). The PLGS use two lasers, at 589 and 569 nm, producing an artificial star with wavelengths as shown in Fig. 1(a). An alternative conceptual PLGS utilizing a single laser tuned to the $4\,P_{3/2}$ Na excitation at 330 nm has also been proposed (Pique, Moldovan & Fesquet 2006) and tested in the laboratory (Moldovan et al. 2007; Chen et al. 2016), to produce an artificial star with wavelengths as shown in Fig. 1(b). As shown in Fig. 1, however, the production ratios between photons of different wavelengths from either 2-laser or 1-laser PLGS are not absolutely mandated by a single direct cascade but, rather, depend on the ratios of different transition strengths and, thus, on uncertainties

[1]Historically, most LGS lasers were dye-based.
[2]Typical LGS return flux is in the range $(5 – 25) \times 10^6$ photons s^{-1} m^{-2}.

[3]In this paper, wavelengths are given in vacuum, typically to either the nearest nanometre, or nearest hundredth of a nanometre. Wavelengths for sodium are as provided by Kelleher & Podobedova (2008).
[4]Other elements with weakly bound outer-shell electrons, such as potassium (which also has strong D-line resonances, at 767 and 770 nm), and calcium (with a strong resonance at 423 nm), have optical transitions of similar strength to the Na D lines, but the paucity of those elements in the Earth's upper atmosphere, relative to Na, reduces their potential for LGS utilization.

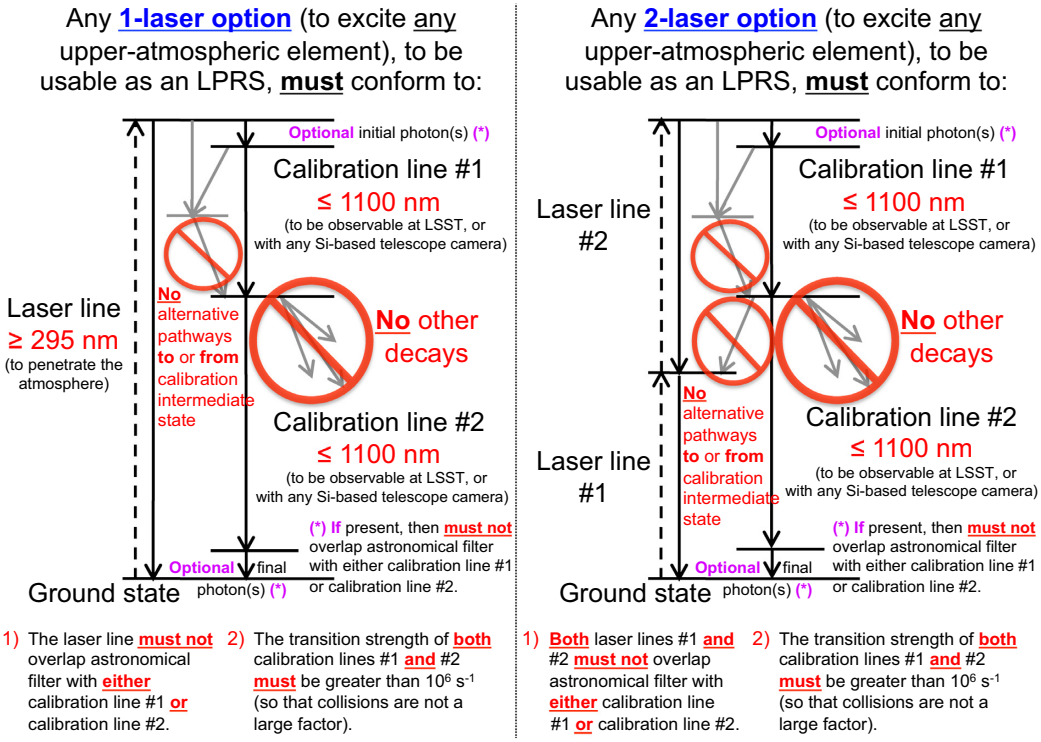

Figure 2. Constraints on atomic level diagrams for an LPRS in the case of one-laser on-resonance excitation (left), and two-laser on-resonance excitation (right).

in the precise knowledge of those transition strengths; whereas the laser photometric ratio star (LPRS) described in the next section and in Fig. 1(c) does not have that limitation. Additionally, an LPRS will produce all of its calibration photons at wavelengths less than the ∼1100 nm maximum wavelength that would be observable with the LSST camera at the Rubin Observatory and other silicon-based optical cameras; whereas all 1138 nm and above photons produced by PLGS are above the maximum Si-observable wavelength.[5]

3 CONCEPT: PRINCIPLE OF LASER PHOTOMETRIC RATIO STARS

As shown in Fig. 1(c), the $3\,D_{3/2}$ state of neutral sodium atoms can be photoexcited by a 342.78 nm laser, resulting in a 'fully-mandated cascade' of two photons: an 819/820 nm photon followed by a 589/590 nm photon.[6] This mandates a 1:1 ratio between production of 819/820 nm photons vs. 589/590 nm photons. We importantly note that the 342.78 nm transition is a 'forbidden' electric quadrupole transition with Einstein A coefficient within[7] the range $(2-7)\times10^2\ s^{-1}$, approximately five orders of magnitude smaller than the (precisely measured) $6.2\times10^7\ s^{-1}$, $1.2\times10^7\ s^{-1}$, and $2.7\times10^6\ s^{-1}$ Einstein A coefficients for the allowed 589, 569, and 330 nm transitions, respectively (Meißner & Luft 1937; Juncar et al. 1981; Kramida et al. 2020). Although the 342.78 nm transition is, thus, much weaker than the 589, 569, or 330 nm transitions that are excited by PLGS lasers, with the use of a powerful (≥500 W average power) laser, 342.78 nm is still definitely a strong enough transition to produce an LPRS for use at the Rubin Observatory and other 8-m class (or larger) telescopes, as calculated below in Sections 6–9.

4 OTHER UPPER-ATMOSPHERIC EXCITATIONS CONSIDERED

To search for alternative artificial sources in the upper atmosphere with precise photometric ratios in the optical domain, which would also be useful for performing relative photometric calibration of

[5]Nevertheless (even if neither 1:1, nor presently known with high precision), the *temporal stability* of the production ratio of 330 nm photons to 589/590 nm photons from a 1-laser PLGS might have some utility for relative photometric calibration between 330 nm and 589/590 nm at observatories; although the time-dependence of near-180° Rayleigh scattering in the lower atmosphere of 330 nm photons from the laser could confound such a photometric-ratio usage of a 1-laser PLGS.

[6]The only other de-excitation option from the $3\,D_{3/2}$ state is the emission of a single photon of the same 342.78 nm wavelength that initially excited the atom. That is an electric quadrupole transition that is suppressed compared to the 819/820 + 589/590 nm photon channel, and also does not affect the 1:1 ratio between 819/820 and 589/590 nm photon production.

[7]The precise value of this Einstein A coefficient has been subject to some controversy: Hertel & Ross (1969) experimentally measured the value $(6.9\pm0.7)\times10^2\ s^{-1}$. A theoretical calculation was then performed by Ali (1971), which agreed with that experimental result. However, a 'substantial error' in the Ali (1971) calculation was noticed by McEachran & Cohen (1973), and the revised theoretical estimate of $2.1\times10^2\ s^{-1}$ resulted, which is just over 3× smaller than the Hertel & Ross (1969) experimental measurement. That discrepancy has not yet been resolved with additional measurements or calculations. We conservatively use the lower $2.1\times10^2\ s^{-1}$ McEachran & Cohen (1973) theoretical estimate throughout this paper.

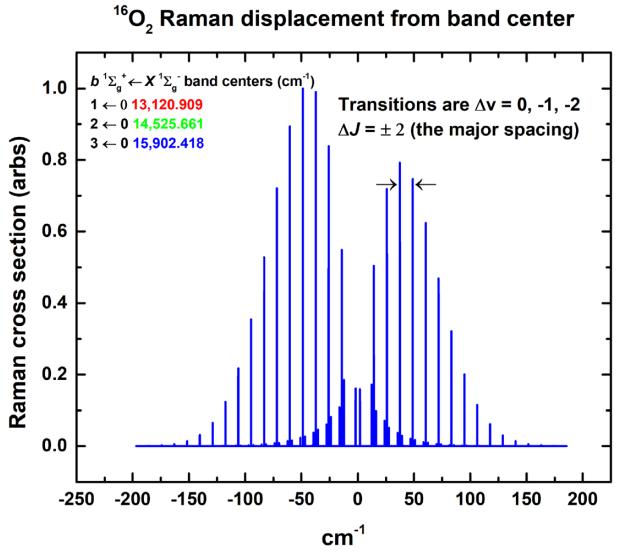

Figure 3. Spectrum of resonant Raman scattering in $^{16}O_2$ in the Schuman–Runge electronic bands [data from Gordon et al. (2017)].

the combined throughput of atmosphere, telescope, and camera between wavelengths in different optical filters, we considered various different possible sets of atmospheric atomic and molecular optical excitations. Figure 2 shows constraints on properties of atomic systems that could be useful for such calibrations, in both one-laser and two-laser on-resonance excitation schemes.

We developed a code, `LPRSAtomicCascadeFinder`,[8] to search the Kramida et al. (2020) data base for sets of atomic transitions that would obey the constraints shown in the Fig. 2 diagrams. In addition to neutral sodium (Na I), we ran `LPRSAtomicCascadeFinder` on the Al I, C I, Ca I, Fe I, H I, He I, K I, N I, Ne I, O I, Al II, C II, Ca II, Fe II, H II, He II, K II, N II, Na II, Ne II, and O II tables from Kramida et al. (2020). The only set of atomic transitions found is the 342.78 nm excitation of Na I [shown in Fig. 1(c) and described in the previous section]. However, please see Albert et al. (2021a; hereafter referred to as Paper II) for two-laser *off-resonance* atomic excitation options for LPRS generation.

In regard to molecular excitations, there are multiple compounds in both the lower and upper atmosphere (for example $^{16}O_2$, as shown in Fig. 3) with spectra with relative wavelengths that are known to extraordinarily high precision (e.g. to a part in 10^7, or even better in some cases). Recently, by using Raman spectroscopy of multiple atmospheric components with scattered light returned from the LGS system of the Very Large Telescope (VLT) at Paranal in Chile, precise calibration of the VLT ESPRESSO spectrograph was achieved (Vogt 2019). However, the relative cross-sections corresponding to the different spectral lines — which are the quantities that are important for relative *photometric*, rather than *spectroscopic*, calibration — are known to far lower precisions: typically of order (5–20)% (Buldakov et al. 1996; Simbotin et al. 1997), and thus unfortunately would not approach the precision of relative photometric calibration using the far more precisely predicted 1:1 photometric ratio of 819/820 nm photons to 589/590 nm photons from 342.78 nm LPRS excitation of the sodium layer.

[8]Available from the authors upon request.

5 LASER AND LAUNCH TELESCOPE

To drive the weak 342.78 nm dipole parity-forbidden transition in neutral sodium, as shown below in Sections 6–9, a powerful (≥500 W average power) laser is required to generate an observable and usable photometric ratio star, even for large telescopes with deep limiting magnitudes, such as at the Rubin Observatory.[9] A 500 W average power 342.78 nm laser with launch telescope is, nevertheless, clearly technologically achievable. In this section, we provide an example set of specifications and a design outline (consisting of two laser design options) for a laser and launch telescope that would meet the requirements for an LPRS for precision photometric calibration for the case of LSST at the Rubin Observatory.

Since the natural linewidth of the 342.78 nm Na I transition is narrow in comparison with the line broadening induced by the thermal motion of the Na I atoms, the maximum optimal laser linewidth will be governed by this Doppler broadening of the transition in the mesosphere:

$$\sigma_\nu \leq \frac{\nu_0}{c}\sqrt{\frac{k_B T_{100\,\mathrm{km}}}{M_{\mathrm{Na}}}} \quad \text{(Doppler broadening)}, \tag{1}$$

where $T_{100\,\mathrm{km}} \approx 200$ K, and will thus be $\sigma_\nu \lesssim 1.5$ GHz (i.e. $\sigma_\nu \lesssim 0.05\ \mathrm{cm}^{-1}$, $\sigma_\lambda \lesssim 0.0006$ nm).

Solid-state laser systems generally are preferable to dye-based systems due to their higher wall-plug efficiencies, lower maintenance requirements, and reduced sensitivity to vibrations and ground movement; however solid-state systems are typically less wavelength-flexible than dye systems, and often require longer design times and can have higher design and construction costs. Advances in optical parametric oscillator (OPO) and in closely related nonlinear optical crystal technology for wavelength flexibility for solid-state lasers, as well as in the output power and linewidth of solid-state near-infrared (NIR) pump lasers (including Yb-doped optical fiber- and disc-based pump laser amplification systems), have largely amelioriated such disadvantages of solid-state systems. Here, we provide two options for solid-state lasers that could meet the challenging average power, linewidth, and wavelength requirements for creating an LPRS for the Rubin Observatory.

The first option uses a 532 nm single-mode quasi-continuous-wave (∼250 MHz repetition rate) frequency-doubled Nd:YAG fiber laser, with an average output power of 1 kW and linewidth of <1 GHz, from IPG Photonics (2021; product VLR-532-1000), as input to a beamsplitter, with one half of the resulting light entering a lithium triborate (LBO) OPO crystal for the production of 963.1 nm light (as well as unused 1188.5 nm light); and this resulting 963.1 nm light, as well as the other half of the 532 nm light, entering a second LBO crystal that acts as a sum-frequency generator (SFG) that combines the 963.1 and 532 nm input photons into 342.7 nm output light. The wavelength of the output light would then be variable between 342.6 and 342.8 nm by a small adjustment of the angle of the OPO crystal. The conversion efficiencies of the OPO and SFG processes can each exceed 50 per cent. Although an optical output power of 500 W at 342.7 nm when using an input power of 1 kW at 532 nm would be difficult to achieve, it would be both possible and made easier by the likely future increases in available input power from single-mode 532 nm pump lasers (from IPG and other suppliers). The cooling of the OPO and SFG crystals would also be an engineering

[9]Per Ivezić et al. (2019), the minimum single-visit limiting magnitudes for astronomical point sources using Rubin *ugrizy* filters will be 23.4, 24.6, 24.3, 23.6, 22.9, 21.7, respectively, with exposure times per visit of 30 s.

challenge with such high average optical input powers, but would not be insurmountable with a carefully designed water cooling system for those optics.

The second option would also use two LBO crystals, also for OPO and SFG processes respectively, for the production of 342.7 nm output light, but would use as input a 515 nm single-mode frequency-doubled 1030 nm Yb-fiber or Yb:YAG disc pump laser (instead of using 532 nm input). High-power 1030 nm Yb pump lasers are available from, for example, TRUMPF (2021; TruDisc product line, which could be made into single-mode lasers) and IPG Photonics (2021; product YLR-1030-1000), which could then be frequency-doubled to 515 nm output with the standard addition of a high-efficiency second-harmonic generation (SHG) crystal. Following the generation of the 515 nm output, the light path would then proceed in a qualitatively similar way to the first option, however with an increase in efficiency from the OPO process, since the necessarily-wasted idler beam would be at a longer wavelength (2071 nm, rather than the 1188.5 nm in the first option), and thus consume less energy. Variability of the output wavelength between 342.6 and 342.8 nm would also proceed in a similar way as in the first option.

Additional conceivable possibilities for producing light with our necessary average output power ($\geq$500 W), linewidth ($\leq$1.5 GHz), and wavelength (variable between 342.6 and 342.8 nm) specifications may include: (a) The frequency-tripling (using a third-harmonic generation crystal) of high-power single-mode input light that could vary in wavelength between 1027.8 and 1028.4 nm (i.e. just below the 1030 nm optimal output wavelength of Yb-fiber or Yb:YAG disc lasers, which could possibly be achieved via a small real-time variation of the properties, such as tension or temperature, of the fiber Bragg grating or the Yb:YAG disc); or (b) The use of a high-output-power frequency-doubled dye laser (rather than the solid-state options above). However, we believe the two options provided in the above paragraphs would be more practical and relatively easier to achieve than either of those possibilities.

The output laser light would be directed into the sky via a low-divergence launch telescope, which expands the beam, and correspondingly lowers its angular divergence, in order to minimize the resulting beam diameter at 100 km altitude. The launch telescope would have the same general optical design as typical launch telescopes for LGS, i.e. expansion of the beam to approximately 0.5 m diameter with the minimum achievable wavefront error, however the optical elements (lens material and mirror coatings) would of course be optimized for 342.8 nm, rather than for 589 nm as in LGS. (Specifically, mirror coatings would be UV-enhanced aluminum;[10] and lens materials would be UV-grade fused silica, MgF_2, or CaF_2, rather than glass.) As the laser input to the launch telescope can achieve a beam quality that is within a factor of 2 of diffraction limitation, the resulting output beam from the launch telescope can achieve an angular divergence that is below 0.2″ (the pixel scale of the LSST camera at the Rubin Observatory).[11]

[10]I.e. similar, for example, to Thorlabs K07 coating (Thorlabs 2021), which is optimized for light near 350 nm and can achieve reflectance of >99% at 0° incidence angle and >98% at 45° incidence angle, at wavelengths between 342.6 and 342.8 nm.

[11]We note that the safety and regulatory aspects of a 500 W laser beam that is outside the visible spectrum would be important. Although the beam would of course be directed into the sky and away from humans, the power of the beam and its resulting Rayleigh-scattered light could potentially cause eye damage or even burned skin if one were physically too close to the beam path, or were to look directly at it from nearby, without any intervening absorber of near-UV light. We estimate that, if near an observatory while such a beam is on, a distance of 50 m from the beam if not looking directly at its path, or at least 500 m away if looking directly at its path without eye protection, will be sufficient for human safety. To prevent humans from entering the open observatory dome when the beam is on, interlocks would clearly need to be placed on doors to the dome. A low-power eye-visible laser beam co-axial with the 342.78 nm beam, with an additional audible alarm both prior to and during beam turn-on, would give proper warning. Birds and other wildlife that happened to fly within the path of the beam could be seriously injured or killed, however fortunately very few birds fly over the top of high-altitude observatory sites at night. Aircraft or satellites that happened to pass through the path of the laser beam would do so extremely quickly and thus absorb very little energy on any given surface, so we view that as less dangerous than humans being outdoors in the near vicinity of the observatory when such a beam is operational.

5.1.1 LPRS size and ellipticity

The resulting diameter of the beam at the 100 km altitude of the sodium layer will approximately equal the sum in quadrature of the beam diameter at launch telescope exit, the expansion of the beam in the atmosphere due to its angular divergence at launch telescope exit, and the expansion of the beam in the atmosphere due to angular divergence caused by atmospheric turbulence. In clear conditions, total atmospheric divergence in a vertical path due to typical amounts of turbulence is at the level of approximately 5 μrad $\approx 1''$ (Tatarski 1961), and thus the beam diameter at 100 km would be, thus, approximately $\sqrt{(0.5)^2 + (0.1)^2 + (0.5)^2}$ m ≈ 0.7 m, i.e. about 1.4″ on the sky.

A small additional enlargement of the LPRS beam diameter in a radial direction outward from the centre of the telescopic field of view would occur, for the reason that, as shown in Fig. 4(a), the centre of the laser launch telescope would be slightly offset from the centre of the aperture of the observing telescope. That, together with the finite extent of the sodium layer in Earth's atmosphere, would result in an additional angular diameter of the LPRS spot, corresponding to the angular diameter of the linear intersection of the laser beam with the vertical extent of the sodium layer. (This effect would be similar and completely analogous to observed ellipticity of LGS, for an identical reason.) The LPRS would thus be approximately elliptical in shape, rather than perfectly circular, on the field of view. We calculate that the resulting eccentricity of the LPRS ellipse would be approximately 0.75 (i.e. that the major axis diameter of the LPRS ellipse will be approximately 2.1″ on the sky, with the minor axis diameter being the previously calculated 1.4″), under simple assumptions that the LPRS beam is launched 4 metres offset from the centre of the telescope aperture, and that the number density of Na I atoms is approximately Gaussian-distributed and centred at 90 km above the elevation of the telescope, with 102.5 and 77.5 km above telescope elevation respectively forming the upper and lower 90 per cent confidence level limits of this Gaussian distribution (i.e. that the standard deviation of the vertical distribution of Na I number density is approximately 8 km).

In the absence of atmospheric turbulence, and with an upward-launched laser beam having a perfectly spatially Gaussian-distributed intensity profile, the LPRS profile would then, in that case — together with the above-mentioned number density of Na I atoms being hypothetically Gaussian-distributed in altitude — be a perfectly Gaussian ellipse on the sky. As shown in, for example, Holzlöhner et al. (2010), real LGS profiles on the sky, and by extension the profile of an LPRS on the sky, will have larger tails and be more complex to precisely parametrize than would a simple 2D Gaussian-distributed spatial profile. However, for the sake of simplicity, we make the assumption in the analysis in Sections 6–9 of this paper that the LPRS

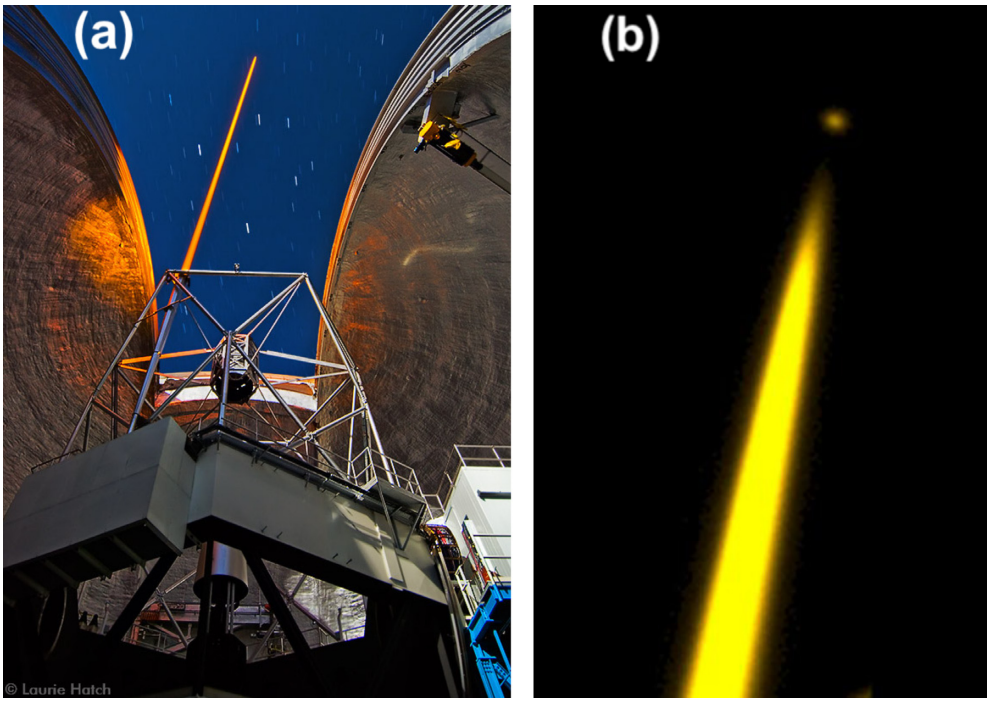

Figure 4. For visualization of the effects of Rayleigh scattering for LGS as well as for LPRS: the Keck II LGS during operation. (a) A photograph (copyright Laurie Hatch, http://lauriehatch.com) of the Keck II LGS physical setup, and (b) An LGS image taken with the Keck II NIRC2 camera. The qualitative aspects of Rayleigh-scattered laser light for an LPRS would, for the most part, be similar to those for this Keck LGS and other sodium LGS, however there are two differences that would tend to make the effects from Rayleigh scattering larger in an LPRS than in an LGS, and a third that would tend to make Rayleigh scattering effects smaller in an LPRS than in an LGS: (1) The relative amount of laser light, to signal light returned from the sodium layer, is 5 orders of magnitude larger for LPRS than for LGS; (2) The cross-section for Rayleigh scattering at 343 nm is approximately nine times greater than at 589 nm; and (3) Rayleigh-scattered 343 nm light is outside of the filter bandpasses of the two LPRS calibration lines near 589 and 819 nm, respectively.

profile on the sky will be a perfectly Gaussian ellipse. Although this will likely tend to slightly overestimate the observed signal flux, and thus slightly underestimate the resulting uncertainty on the observed photometric ratio, we feel that the resulting corrections from these effects to the analysis performed in this paper are likely to be small.

5.1.2 Flat-fielding

Uncertainties related to the flat-fielding of photometric calibration data across the full focal plane can also constitute a significant component of systematic uncertainty for SNeIa dark energy and other measurements (Wood-Vasey et al. 2007; Betoule et al. 2014; Jones et al. 2018). With the laser launch telescope rigidly affixed to the main telescope outer support structure as in Fig. 4(a), the resulting LPRS would be in a fixed location on the focal plane, and thus the LPRS would not address such uncertainties related to flat-fielding. However, if the launch telescope were instead mounted to the main telescope structure on a tip-tilt mount, so that the launch telescope could slightly tip and tilt in altitude and azimuth with respect to the main telescope (up to approximately a degree in the two directions), the LPRS could then be moved around the focal plane as needed in order to ameliorate flat-fielding uncertainties.

5.1.3 Intra-filter relative spectrophotometry

The LPRS techniques described in this paper, as well as in Paper II, can provide precise int*er*-filter calibration constants to quantify the total relative throughput of atmosphere, telescope, camera, and detector at 589/590 nm wavelengths (at which the *r* filter would be used) vs. at 819/820 nm wavelengths (at which the *i* or *z* filter would be used). Int*ra*-filter calibration constants, to quantify the total throughput ratio between pairs of wavelengths within the bandpass of any single filter (or between any pairs of filters other than *r* vs. *i* or *z*), would need to be determined via other calibration methods.[12] Stellar standards provide the typical means (e.g. Bohlin & Gilliland 2004; Holberg & Bergeron 2006) for such other calibrations [in addition to individual laboratory characterization of filter, detector, camera, and telescope optical spectral response, as described in Stubbs & Tonry (2006), Doi et al. (2010), and other references]. Another technique for characterizing combined relative throughput of telescope, camera, and detector, but not of the atmosphere, at pairs of wavelengths across the optical spectrum is described in Stubbs et al. (2010); and general techniques presently under development for precisely measuring total throughput, and performing both relative and absolute spectrophotometry, are described in Albert (2012) and in Albert, Brown & Stubbs (2021b). Conceivably, the upper-atmospheric Rayleigh backscattering of light launched into the sky from a broadly-tunable laser — and continuously monitored via a calibrated photodiode that receives a constant small fraction of the laser light from a beamsplitter at this laser source — could also be used for characterizing combined relative throughput; although such a technique has, to our knowledge, never been published. The LPRS techniques we describe in this pair

[12] Absolute photometry, i.e. an overall absolute flux scale — while less critical for most present astrophysical results (for example, measurements of dark energy using SNeIa are largely independent of overall absolute flux scale) — would also not be addressed with an LPRS, and thus would also need to be determined using other methods.

of papers are, thus, not the only techniques one would need to satisfy all spectrophotometric calibration requirements; however they would provide a very high-precision reference to pinpoint the total relative throughput at 589/590 vs. 819/820 nm.

5.1.4 Laser pulse repetition rate; and pulse chirping

The pump laser for the LPRS will be pulsed at a high frequency, such as the repetition rate of ∼250 MHz for the IPG VLR-532-1000 mentioned earlier in this section. In order to maximize the brightness of the LPRS (Kane, Hillman & Denman 2014), this repetition rate could be adjusted (and also re-adjusted as often as is practical) to be an integer multiple of the Na atomic Larmor frequency

$$f_{\rm Na,\,Larmor} \equiv \frac{\gamma_{\rm Na}}{2\pi} B, \tag{2}$$

where the ground-state gyromagnetic ratio for sodium is $\frac{\gamma_{\rm Na}}{2\pi} = 699.812$ kHz/gauss. For typical geomagnetic field strengths of $B = 0.25$ gauss to 0.5 gauss, $f_{\rm Na,Larmor}$ can range between 175 and 350 kHz (with a typical value being $f_{\rm Na,Larmor} \approx 260$ kHz), and thus it would not be difficult to adjust the very high (∼250 MHz) and continuously-adjustible repetition rate of the pump laser to be an integer multiple of $f_{\rm Na,Larmor}$. Either alternatively to, or in combination with, this adjustment of the pump laser repetition rate, the laser output can have circular polarization orientation (σ_+ or σ_-) that is modulated at $f_{\rm Na,Larmor}$ or an integer multiple thereof, in order to achieve a similar LPRS brightness-increasing effect (Fan, Zhou & Feng 2016; Pedreros Bustos et al. 2018). Although, in contrast to typical LGS, only a very small fraction of the Na I atoms in the sodium layer will be excited by the laser at any given time in this LPRS, it would still be at least slightly beneficial to use these Larmor frequency techniques to close the excitation/de-excitation cycle between a specific pair of hyperfine states for a given Na I atom, for the small fraction of Na I atoms in this LPRS that happen to repeat the cycle. Another technique that also has the potential to at least marginally increase LPRS brightness is the chirping of the frequency of LPRS pulses, similar to LGS continuous wave (CW) laser chirping as described in Pedreros Bustos et al. (2020). Although this LPRS laser will be a rapidly-pulsed quasi-CW (QCW) source, rather than a CW source, the technique described in Pedreros Bustos et al. (2020) may be also applicable to a QCW LPRS by using frequency chirping either within each single pulse, or having the frequency increase during each chirp continue during a train of multiple pulses. However, in our estimations of observed flux and of impact on measurements of dark energy in the following sections, we do not assume that any of the possible LPRS brightness-increasing techniques described in this paragraph have been implemented.

6 ESTIMATION OF OBSERVED SIGNAL FLUX FROM LPRS

In this section, we calculate the expected observed flux at an observatory, for example the Rubin Observatory, which is located at the same mountaintop site as a source laser with properties described in the previous section, from the resulting de-excitation light generated in the sodium layer in the mesosphere. For a laser with 500 W average output power that is tuned to the $\lambda_s \equiv 342.78$ nm Na I excitation, the number of photons produced per second by the laser will be $N_\gamma^{\rm laser} \equiv \frac{P\lambda_s}{hc} = \frac{(500\ {\rm W})\times(3.4278\times10^{-7}\ {\rm m})}{(6.63\times10^{-34}\ {\rm J\,s})\times(3.0\times10^{8}\ {\rm m\,s^{-1}})} = 8.61\times10^{20}$ photons s^{-1}. The atmospheric transmission above the 2663 m Cerro Pachon site (the Rubin Observatory site, as our example) at 342.78 nm is approximately 60 per cent (with losses dominated by Rayleigh scattering) in a vertical path, thus the number of 342.78 nm photons that reach the upper atmosphere per second will be approximately $N_\gamma^{\text{laser-to-mesosphere}} \equiv 0.60 \times N_\gamma^{\rm laser} = 5.17 \times 10^{20}$ photons s^{-1}. Of these $N_\gamma^{\text{laser-to-mesosphere}} = 5.17\times10^{20}$ photons each second, a small fraction will be absorbed by Na I atoms in the mesosphere; we determine this fraction in the following. As was mentioned in Section 2, the total column density of neutral sodium atoms varies within a range of approximately $(2-8)\times10^9$ atoms cm^{-2}; we shall use 4×10^9 atoms cm^{-2} $= 4\times10^{13}$ atoms m^{-2} in our calculation. The total absorption cross-section per ground state Na I atom $\sigma_{342.78\ {\rm nm}} = \frac{c^2}{8\pi\nu_{ki}^2}\frac{g_k}{g_i}\phi_\nu A_{ki}$, where $A_{ki} = 2.1\times10^2$ s^{-1} is the Einstein A coefficient,[7] $\nu_{ki} = \frac{c}{342.78\ {\rm nm}} = 1.14\times10^{15}$ s^{-1}, the level degeneracy ratio $\frac{g_k}{g_i} = \frac{4}{2} = 2$ and $\phi_\nu \approx \frac{1}{1.5\ {\rm GHz}} = 6.67\times10^{-10}$ s. Thus $\sigma_{342.78\ {\rm nm}} \approx 7.74\times10^{-22}$ m^2 per atom, and thus each 342.78 nm photon has an approximately $7.74\times10^{-22}\times4\times10^{13} = 3.10\times10^{-8}$ chance of exciting an Na I atom. There will thus be approximately $3.10\times10^{-8}\times N_\gamma^{\text{laser-to-mesosphere}} =$

$$1.6\times10^{13}\ {\rm Na\,I\ atoms\ excited\ per\ second} \tag{3}$$

in the mesosphere.

Each of those excited Na I atoms will emit one 818.55 or 819.70 nm photon, as well as one 589.16 or 589.76 nm photon, within approximately 100 ns, with the photons emitted in uniform angular distributions. The atmospheric transmission back down to the 2663 m Cerro Pachon site at wavelengths of ∼819 and ∼589.5 nm is approximately 90 per cent in the case of both of those wavelengths (with losses dominated by water vapour absorption and by Rayleigh scattering respectively), and thus at the telescope approximately 95 km below the sodium layer, this will correspond to approximately $N_\gamma^{\rm signal} \equiv 0.9\times(1.6\times10^{13})\times\frac{1}{4\pi\times(9.5\times10^4)^2} =$

$$127\ {\rm photons/s/m^2} \tag{4}$$

at each of 818.55 or 819.70 nm, and 589.16 or 589.76 nm.

The apparent magnitude $m \equiv -2.5\log_{10}(\frac{\phi}{\phi_0})$, and in the AB reference system $m_{\rm AB} \equiv -2.5\log_{10}(\phi) - 48.6$ when the spectral flux density ϕ is provided in units of erg s^{-1} cm^{-2} Hz^{-1}. The bandwidths b of the Rubin Observatory r and z filters are approximately (549–694) and (815–926) nm, respectively, which correspond to approximate bandwidths of $b^{r\,\rm band} = 1.14\times10^{14}$ and $b^{z\,\rm band} = 4.41\times10^{13}$ Hz, respectively. These filter bandwidths must be multiplied by filter spectral ratios $f \equiv$ (average filter throughput over the band)/(filter throughput at the wavelength of the nearly monochromatic light) to account for the 818.55/819.70 nm light being near the edge of the z band, whereas the 589.16/589.76 nm light is near the centre of the r band; $f_{589.5\ {\rm nm}}^{r\,\rm band} = \frac{0.881}{0.943} = 0.934$ and $f_{819\ {\rm nm}}^{z\,\rm band} = \frac{0.851}{0.501} = 1.699$, and thus the corrected effective bandwidths are $f_{589.5\ {\rm nm}}^{r\,\rm band}\times b^{r\,\rm band} = 1.06\times10^{14}$ Hz and $f_{819\ {\rm nm}}^{z\,\rm band}\times b^{z\,\rm band} = 7.49\times10^{13}$ Hz, respectively. At a wavelength of 589.5 nm, 127 photons s^{-1} m^{-2} corresponds to 4.29×10^{-14} erg s^{-1} cm^{-2}, and at a wavelength of 819 nm, 127 photons s^{-1} m^{-2} corresponds to 1.55×10^{-14} erg s^{-1} cm^{-2}. Thus, for an LPRS, $\phi^{r\,\rm band} = (4.29\times10^{-14}\ {\rm erg\,s^{-1}\,cm^{-2}})/(1.06\times10^{14}\ {\rm Hz}) = 4.05\times10^{-28}$ erg s^{-1} cm^{-2} Hz^{-1} and $\phi^{z\,\rm band} = (3.08\times10^{-14}\ {\rm erg\,s^{-1}\,cm^{-2}})/(7.49\times10^{13}\ {\rm Hz}) = 4.11\times10^{-28}$ erg s^{-1} cm^{-2} Hz^{-1}; and thus

$$m_{\rm AB}^{r\,\rm band} = 19.9, \quad \text{and} \tag{5}$$

$$m_{\rm AB}^{z\,\rm band} = 19.9 \tag{6}$$

for an LPRS. Since 819 nm light lies in the overlap region between the Rubin i and z filters, light from the LPRS will additionally be (more

dimly) observable in the Rubin i band. An analogous calculation to the above thus gives $\phi^{i\,\mathrm{band}} = (3.08 \times 10^{-14}\,\mathrm{erg\,s^{-1}\,cm^{-2}})/(1.43 \times 10^{14}\,\mathrm{Hz}) = 2.15 \times 10^{-28}\,\mathrm{erg\,s^{-1}\,cm^{-2}\,Hz^{-1}}$ and

$$m_{\mathrm{AB}}^{i\,\mathrm{band}} \;=\; 20.6 \tag{7}$$

for an LPRS.

As determined above, the flux of LPRS signal photons incident on the telescope is 127 photons $\mathrm{s^{-1}\,m^{-2}}$ at each of 819 and 589 nm, which would correspond to 4445 photons $\mathrm{s^{-1}}$ at each of those two wavelengths in the specific case of the 35 $\mathrm{m^2}$ clear aperture of the Simonyi Survey Telescope at the Rubin Observatory. Using the expected Rubin values for instrumental optical throughput and detector quantum efficiency (Jones et al. 2019), this corresponds to total numbers of observed signal photoelectrons equal to 5.73×10^4, 2.40×10^4, and 3.73×10^4 within the elliptical LPRS spot (with the previously calculated major and minor axis angular diameters of $2.1'' \times 1.4''$) during a 30 s visit, in Rubin r, i, and z filters, respectively. That corresponds to averages of 959, 402, and 625 signal photoelectrons per $0.2'' \times 0.2''$ LSST camera pixel at the centre of the Gaussian spot in that time interval; i.e. signal standard deviations at the centre of the Gaussian spot of approximately $\sqrt{959} = 31.0$, $\sqrt{402} = 20.0$, and $\sqrt{625} = 25.0$ photoelectrons per pixel per visit in the Rubin r, i, and z filters respectively.

In any forseeable application of this technique, the dominant uncertainty on the relative amount of light from 818.55/819.70 vs. 589.16/589.76 nm signal photons would be due to the Poisson uncertainties on small-sample collected photon statistics,[13] and the analogous binomial uncertainty on their ratio. However, given hypothetical infinite photon statistics, one might ask just how well the 1:1 ratio is predicted, i.e. what the dominant systematic uncertainty on that signal ratio would be. We estimate that the dominant systematic uncertainty on the 1:1 signal ratio would, by far, be due to collisions of the neutral sodium atoms in the upper atmosphere during de-excitation: inelastic collisions of the excited atoms could potentially eliminate the production of (or dramatically modify the wavelength of) either the 818.55/819.70 or the 589.16/589.76 nm photon during a given de-excitation. The typical frequency of atomic collisions of a given sodium atom at the ∼100 km altitude of the sodium layer is

$$\nu_{\mathrm{collision}} \;=\; 4 n_{100\,\mathrm{km}} \langle\sigma\rangle \sqrt{\frac{k_B T_{100\,\mathrm{km}}}{\pi m_{\mathrm{Na}}}} \;\approx\; 770\ \mathrm{s^{-1}}, \tag{8}$$

where $n_{100\,\mathrm{km}} \approx 10^{19}\,\mathrm{m^{-3}}$ is the total number density of all species at 100 km altitude, $\langle\sigma\rangle \approx \pi \times (2 \times 10^{-10}\,\mathrm{m})^2 = 4\pi \times 10^{-20}\ \mathrm{m^2}$ is an averaged cross-sectional area for the collisional interaction of an Na I atom with any other species at that altitude, and $T_{100\,\mathrm{km}} \approx$ 200 K. The Einstein A coefficients of the 818.55, 819.70, 589.16, and 589.76 nm transitions range from $A_{\mathrm{min}} = 8.57 \times 10^6\ \mathrm{s^{-1}}$ to $A_{\mathrm{max}} = 6.16 \times 10^7\ \mathrm{s^{-1}}$, so we can set an upper bound on the fractional expected systematic deviation from a 1:1 ratio of 818.55/819.70 vs. 589.16/589.76 nm signal photons as

$$\epsilon \;\equiv\; \frac{\nu_{\mathrm{collision}}}{A_{\mathrm{min}}} \;=\; 9 \times 10^{-5}, \tag{9}$$

so that the ratio together with its systematic uncertainty becomes $(1 \pm \epsilon)$:1. (This bound could conceivably be made yet tighter via a detailed simulation of collisional processes.)

[13] Also known as shot noise.

7 ESTIMATION OF LPRS OBSERVED BACKGROUND

Observed light from an LPRS will be superimposed on two types of background light: (*a*) Laser-induced background light; and (*b*) The typical diffuse sky background (which we, as is usual, take to include all other [i.e. non-laser] light that is scattered by the optical elements of the telescope, as well as by the atmosphere and by zodiacal dust), plus instrumental background noise. In this section, we estimate the size of contributions from both of these sources of background: in particular we show that type (*a*) may indeed be quite significant unless (342.6–342.8) nm light can be rejected by the r, i, and z filters at a level (optical density [OD] of >6.7) that is significantly greater than the present Rubin filter specifications, and that type (*b*), the background over which all objects are observed, will be corrected through the usual technique of sky subtraction.

For type (*a*), potential laser-induced background light can itself be divided into two categories: (a_1) The background light from near-180° atmospheric Rayleigh scattering of the 342.78 nm laser light that also manages to pass through the r, i, or z filters (via an imperfect rejection of 342.78 nm light by those filters); and (a_2) The background light from near-180° atmospheric Raman scattering and de-excitation light from other inelastic excitations of atmospheric atoms and molecules in the laser's path, within the passbands of the r, i, or z filters. As we will calculate below, near-180° Rayleigh scattering will result in a large flux of 342.78 nm photons into the telescope aperture, and thus to reduce background of type (a_1) to a negligible level, this technique would require the thorough rejection of 342.78 nm photons (at OD > 6.7) by the r, i, and z filters.

The product of the Rayleigh backscattering cross-section σ_b^R with atmospheric molecular density $n(z)$ can be approximated by the convenient formula:

$$\sigma_b^R n(z) \;=\; (3.6 \times 10^{-31}) \frac{p(z)}{T(z)} \lambda^{-4.0117}\ \mathrm{m^{-1}sr^{-1}}, \tag{10}$$

where $p(z)$ is the pressure in millibars at an altitude z above sea level, $T(z)$ is the temperature in Kelvin at altitude z, and both z and λ are in units of metres (Cerny & Sechrist 1980). Using a roughly approximate isothermal atmosphere model $\frac{p(z)}{T(z)} \approx \frac{p_0}{T_0} e^{-\left(\frac{\mu g z}{R T_0}\right)} \approx \frac{1000}{300} e^{-\left(\frac{z}{8800}\right)}$, we can integrate equation (10) over both the altitude above the 2663 m telescope site and by the solid angle that is subtended by the telescope aperture to obtain an approximate fraction of laser photons that are Rayleigh-backscattered by the atmosphere into the aperture of the telescope:

$$\begin{aligned} f_{b,\mathrm{total\ streak}}^{R,\gamma} &\approx \frac{20\pi \times (3.6 \times 10^{-31}) \times (3.428 \times 10^{-7})^{-4.0117}}{3} \\ &\quad \times \int_{z=2663}^{\infty} e^{-\left(\frac{z}{8800}\right)} dz \int_{\theta=0}^{\tan^{-1}\left(\frac{r}{z-2663}\right)} \sin\theta\, d\theta \\ &\approx 2 \times 10^{-3}, \end{aligned} \tag{11}$$

where $r = 4$ m is the radius of the telescope aperture. That would naively indicate that the r, i, and z filters would need to filter out at the very least $1 - \frac{N_\gamma^{\mathrm{signal}}}{f_{b,\mathrm{total\ streak}}^{R,\gamma} N_\gamma^{\mathrm{laser}}} \approx 1 - (7.4 \times 10^{-17})$ of all such photons, i.e. have OD of $-\log_{10}(7.4 \times 10^{-17}) = 16.1$ for $\lambda \in$ (342.6–342.8) nm. However, since, as shown in Fig. 4(a), the centre of the laser launch telescope would be slightly offset from the centre of the aperture of the observing telescope, the large majority of those Rayleigh-backscattered laser photons that enter the telescope aperture, even if they also manage to get through the r, i, or z filter, would not be directly superimposed on the signal photons returned from the sodium-layer LPRS; the Rayleigh-backscattered

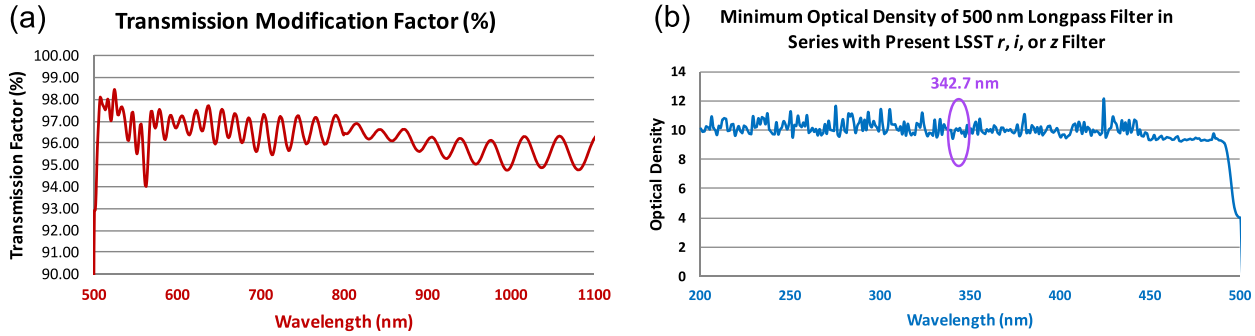

Figure 5. (a) The percentage of transmission that is preserved (relative to present Rubin filters), as a function of wavelength from 500 to 1100 nm; and (b) The minimum OD when out of bandpass, as a function of wavelength from 200 to 500 nm, for a longpass filter with cutoff wavelength of 500 nm, when in series with the present Rubin *r*, *i*, or *z* filter. The present Rubin filters have specifications of minimum OD of 4 when out of bandpass; the addition of such a longpass filter in series with the Rubin *r*, *i*, or *z* filter would raise the OD to greater than 10 for (342.6–342.8) nm, while preserving more than 94 per cent of present light at all in-bandpass wavelengths for each of those three filters. This longpass filter data from Thorlabs (2021; product FELH0500).

light instead tends to form a streak that 'leads up' to the light that is returned from the sodium layer, as shown for example in Fig. 4(b), but is not actually superimposed on the LPRS spot. Thus, the only such Rayleigh-backscattered background photons that would, in fact, be superimposed on the photons from the LPRS on the focal plane (if such photons happened to get through the *r*, *i*, or *z* filter) would be photons that are Rayleigh-backscattered from the same altitude range as the sodium layer itself, i.e. from between 80 and 105 km above sea level:

$$f^{R,\gamma}_{b,\text{over LPRS spot}} \approx \frac{20\pi \times (3.6\times10^{-31}) \times (3.428\times10^{-7})^{-4.0117}}{3} \times \int_{z=80\,000}^{105\,000} e^{-\left(\frac{z}{8800}\right)} \mathrm{d}z \int_{\theta=0}^{\tan^{-1}\left(\frac{r}{z-2663}\right)} \sin\theta \mathrm{d}\theta \approx 7\times10^{-13}, \quad (12)$$

and thus the *r*, *i*, and *z* filters only must filter out at very least $1-\frac{N^{\text{signal}}_{\gamma}}{f^{R,\gamma}_{b,\text{over LPRS spot}}N^{\text{laser}}_{\gamma}} \approx 1-(2.1\times10^{-7})$ of all such photons, i.e. have OD of at very least $-\log_{10}(2.1\times10^{-7}) = 6.7$ for $\lambda \in$ (342.6–342.8) nm. This requirement, while still stringent, is vastly less stringent than a requirement of OD of more than 16. However, the baseline Rubin filter specification only requires that the Rubin filters reject of out-of-band light at OD > 4 (Ivezić et al. 2019) and, thus, achieving a notch rejection of OD > 6.7 for $\lambda \in$ (342.6–342.8) nm light would likely require a future upgrade of those three Rubin filters. Such an upgrade of those filters would not be technically difficult to achieve; for example a standard longpass filter [such as, e.g., product FELH0500 from Thorlabs (2021)] to remove wavelengths below 500 nm in series with the present *r*, *i*, and *z* filters would preserve more than 94 per cent of all present pass-through light across all within-bandpass wavelengths in all three filters, while simultaneously achieving a total OD of greater than 10 for (342.6–342.8) nm light, as shown in Fig. 5. Single combination longpass *r*, *i*, and *z* wavelength filters could likely be produced with the same physical thicknesses and bandpasses as those present Rubin filters, but also combining the strong rejection of $\lambda < 500$ nm light of the longpass filter.[14]

Laser-induced background of type (a_2), i.e. near-180° atmospheric Raman scattering and other inelastic collisions of 342.78 nm laser light into the passbands of the *r*, *i*, or *z* filters, would systematically affect LPRS-based photometric calibration. In particular, molecular oxygen has a column density which is more than 10 orders of magnitude larger than the Na I column density in the sodium layer. Photons scattered from O_2 with wavelengths of 762 and 688 nm arise from spin-forbidden transitions, and while Raman lines in the Schumann–Runge bands are strong, the above lines produce cross-sections of approximately 10^{-40} cm^2 per molecule, and can therefore safely be ignored.

The recent observations, using the 4 Laser Guide Star Facility (4LGSF; Calia et al. 2014), of O_2 and N_2 Raman rotational transitions corresponding to the first vibrational excitation in these molecules (Vogt et al. 2017), reveal that at the maximum of resonant Raman signal for the $\Delta J = 0$ transitions, the line intensity is approximately 10^{-16} erg s^{-1} cm^{-2}. Line intensities due to off-resonant scattering from light at 343 nm will be several orders of magnitude smaller than that value, and thus will be negligible when compared with the returned signal flux from the sodium layer (which has an intensity at 589.16/589.76 nm calculated in Section 6 of approximately 4.29×10^{-14} erg s^{-1} cm^{-2}).

The typical non-laser-induced diffuse sky background, i.e. background of type (*b*), would be corrected via standard techniques of sky subtraction. As was shown in Section 5, the elliptical LPRS spot would have a major axis of approximately 2.1″ angular diameter and minor axis of approximately 1.4″ angular diameter on the sky, which is only slightly larger than the PSF of the LSST camera at the Rubin Observatory when including effects of atmospheric seeing, which is approximately 1″ angular diameter in total (Ivezić et al. 2019). The sky brightness at the zenith in the case of the Rubin Observatory site is estimated to be, in magnitude per square arcsec, 21.2, 20.5, and 19.6 for the *r*, *i*, and *z* filters, respectively (Jones 2017), which corresponds to approximately 1498, 2151, and 3544 photons s^{-1} arcsec^{-2} for the three filters respectively, thus 3459, 5141, and 8472 photons s^{-1} within an elliptical spot of angular diameter 2.1″ × 1.4″.

[14] Alternatively, polarization filters, rather than (or even in addition to) longpass wavelength filters, could be used to greatly reduce laser atmospheric Rayleigh-backscattered light. However, such filters would necessarily only admit light from one polarization from astronomical sources, as well as from the LPRS, which may be unwanted for some astronomical observations. In relation to this, Paper II considers an alternative LPRS generation scheme, which (unlike the scheme in this paper) would necessarily require polarizing filters to be installed, however would provide a brighter LPRS than the technique described in this paper.

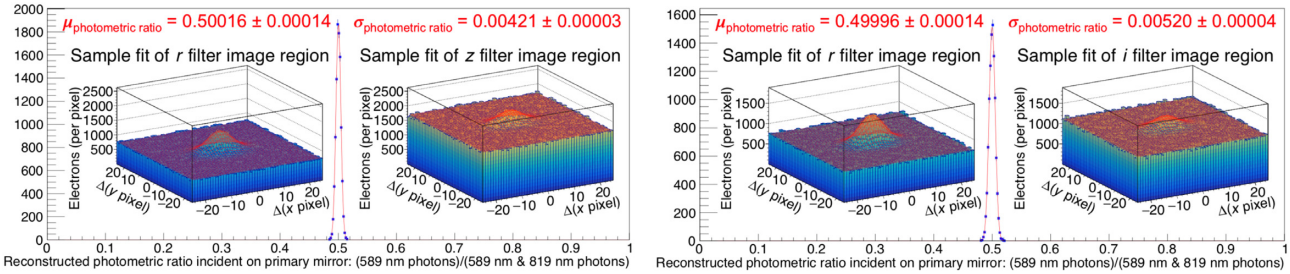

Figure 6. Within both the left and right sets of plots above, the main plot (i.e. the 1D fitted Gaussian curve in the centre of each set of plots) shows the distribution of 10 000 fitted photometric ratios, with each ratio reconstructed from pairs of simulated *r* and *z* filter image regions (within the set of plots on the left-hand side above), and pairs of simulated *r* and *i* filter image regions (within the set of plots on the right-hand side above). For both the left and right sets of plots, each one of the 4 × 10 000 simulated image regions (in total) consists of a 50 pixel × 50 pixel square centred around the observed LPRS centroid. The inset plots show single examples of simulated *r* and *z* filter image regions (within the set of plots on the left), and simulated *r* and *i* filter image regions (within the set of plots on the right), and their respective fits to 2D Gaussian ellipses plus flat background distributions. The photoelectrons and noise electrons in each simulated pixel, in each region, are generated according to the statistical distributions expected from a single 30 s Rubin visit consisting of a pair of 15 s exposures. The fitted number of signal photoelectrons is extracted from each image region fit, and divided by the (photoelectron)/(incident photon) efficiency (consisting of the expected detector quantum efficiency of the LSST camera at the Rubin Observatory, multiplied by the expected throughput fraction of telescope, camera, and filter optics, at 589 and 819 nm for the simulated *r*, *z*, and *i* filter image regions respectively), to determine the reconstructed numbers of 589 and 819 nm photons incident on the Rubin Observatory primary mirror during the 30 s visit. For each simulated image region pair, the resulting ratio of reconstructed (589 nm photons)/(589 nm photons + 819 nm photons) is plotted, and the resulting distribution is fitted to a single Gaussian. The standard deviation of the fit that is shown in the main plot within the *left* set of plots above, which corresponds to the expected LPRS photometric ratio statistical uncertainty from a single pair of visits with the *r* and *z* filter, is equal to 0.004 21 ± 0.000 03, and the mean of the fit is consistent with 0.5. The standard deviation of the fit that is shown in the main plot within the *right* set of plots above, which corresponds to the expected LPRS photometric ratio statistical uncertainty from a single pair of visits with the *r* and *i* filter, is equal to 0.005 20 ± 0.000 04, and the mean of that fit is also consistent with 0.5.

When using the expected Rubin values for instrumental optical throughput and detector quantum efficiency as functions of wavelength (Jones et al. 2019), those values of 3459, 5141, and 8472 photons s^{-1} correspond to total numbers of observed sky background photoelectrons equal to 4.46×10^4, 6.63×10^4, and 1.07×10^5 within the elliptical spot during a 30 s visit consisting of two 15 s exposures, in the *r*, *i*, and *z* filters, respectively. This corresponds to 747, 1110, and 1701 photoelectrons per $0.2'' \times 0.2''$ pixel in that time interval; i.e. sky background standard deviations of approximately $\sqrt{747} = 27.3$, $\sqrt{1110} = 33.3$, and $\sqrt{1701} = 41.2$ photoelectrons per pixel per visit in the *r*, *i*, and *z* filters, respectively. In the same 30 s visit time interval, the expected standard deviation in each pixel due to instrumental background noise (in each of the filters of course) is 12.7 photoelectrons (Jones 2017).

8 RESULTING ESTIMATED PHOTOMETRIC RATIO PRECISION

We determine the resulting estimated photometric ratio measurement precision in the case of utilizing a pair of 30 s LPRS visits in the Rubin *r* and *z* filters, and also in the case of utilizing a pair of visits in the Rubin *r* and *i* filters, in two ways: (1) Using a simple analytic approximation via error propagation; and (2) Using a more detailed numerical determination, using sets of simple Monte Carlo simulations with the ROOT software package (Brun & Rademakers 1997; Antcheva et al. 2011). Both of these estimates assume that Rayleigh-scattered out-of-band 343 nm laser photons are fully blocked from entering the *r*, *i*, or *z* filter images, via longpass upgrades of those three filters, as described in the previous section.

We first make simple analytic approximations of the precision of measurements of the photometric ratio (589 nm photons)/(589 nm photons + 819 nm photons) using pairs of 30 s visits to the LPRS spot, per (1). Let the reconstructed number of 589 nm photons incident on the primary mirror during a 30 s *r* filter visit equal $\rho \pm \delta_\rho$, and the reconstructed number of 819 nm photons incident on the primary mirror during a 30 s *z* filter visit equal $\zeta \pm \delta_\zeta$. We are then measuring the ratio $\frac{\rho \pm \delta_\rho}{(\rho \pm \delta_\rho)+(\zeta \pm \delta_\zeta)}$ which, via error propagation, is equal to $\frac{\rho}{\rho+\zeta} \pm \frac{\zeta\delta_\rho + \rho\delta_\zeta}{(\rho+\zeta)^2}$, when $\frac{\delta_\rho}{\rho}$ and $\frac{\delta_\zeta}{\zeta}$ are both small and the uncertainties are both uncorrelated and Gaussian distributed. From the calculations in Section 6, ρ and ζ will both be equal to approximately $30 \times 4445 = 133\,350$ photons. The uncertainties δ_ρ and δ_ζ will approximately equal the square root of the total number of electrons measured within the detector area of the LPRS spot during the respective visits, each scaled by the ratio of incident photons to measured signal photoelectrons (i.e. by the inverse of the telescope throughput fraction [including detector quantum efficiency]) at the respective wavelengths of 589 and 819 nm. Using the calculations in Sections 6 and 7, we can see that δ_ρ will be approximately $\sqrt{57\,300 + 44\,600} \times \frac{133\,350}{57\,300} = 742.9$ photons and δ_ζ will be approximately $\sqrt{37\,300 + 107\,000} \times \frac{133\,350}{37\,300} = 1358.1$ photons, and thus $\frac{\rho}{\rho+\zeta} \pm \frac{\zeta\delta_\rho + \rho\delta_\zeta}{(\rho+\zeta)^2} \approx 0.5 \pm 0.003\,94$, i.e. a fractional uncertainty of just under a part in 100. A similar calculation for a pair of visits in the *r* and *i* filters (rather than in the *r* and *z* filters) yields $(\iota \pm \delta_\iota) \approx (133\,350 \pm 1670)$ photons, and thus $\frac{\rho}{\rho+\iota} \pm \frac{\iota\delta_\rho + \rho\delta_\iota}{(\rho+\iota)^2} \approx 0.5 \pm 0.004\,52$, also an uncertainty of just under a part in 100, and just slightly larger than when using a pair of visits in the *r* and *z* filters. As we will see, these simple analytic approximations only slightly underestimate the statistical uncertainties, when they are compared with numerical simulations.

Figure 6 shows the results of sets of numerical simulations, per method (2), to determine the precision of photometric ratio measurement using single pairs of visits to the LPRS spot. As shown in this figure, and in the description in its caption, the resulting estimates of the photometric ratio measurement and its statistical uncertainty are 0.5 ± 0.004 21 (the analytic approximation above gave 0.5 ± 0.003 94), and 0.5 ± 0.005 20 (the analytic approximation above gave 0.5 ± 0.004 52), for pairs of visits in the *r* and *z* filters, and in the *r* and *i* filters, respectively.

Those statistical uncertainties could, of course, be reduced by utilizing more than a single pair of visits, at the cost of increased

observation time. Increasing the average optical output power of the LPRS laser above the nominal 500 W would also reduce the statistical uncertainties, by increasing the number of observed LPRS photons.

9 ESTIMATED IMPACT ON MEASUREMENTS OF DARK ENERGY FROM TYPE IA SUPERNOVAE

We estimate the impact of the improved photometry, when utilizing the photometric ratios provided by this LPRS at a survey observatory such as the Rubin Observatory, on future measurements using SNeIa of the dark energy equation of state as a function of redshift $w(z)$. The function $w(z)$ is defined as:

$$w(z) \equiv p_{\rm DE}(z)/\rho_{\rm DE}(z), \tag{13}$$

where $p_{\rm DE}(z)$ and $\rho_{\rm DE}(z)$ are, respectively, the pressure and the energy density of dark energy, both in dimensionless units, as functions of redshift z (under the typical assumption that dark energy behaves as a perfect fluid). In our simulations, we use the usual parametrization (Linder 2003):

$$w(z) = w_0 + \frac{z}{1+z} w_a, \tag{14}$$

where the quantities w_0 and w_a, respectively, parametrize the equation of state of dark energy at the present time, and the amount of change in the equation of state of dark energy over cosmic history. If dark energy is a cosmological constant, then $(w_0, w_a) = (-1, 0)$.

The most commonly-used figure of merit $\mathcal{F}_{\rm DE}$ at present to characterize the performance of a measurement of the properties of dark energy is the inverse area of the uncertainty ellipse in the (w_0, w_a) plane:

$$\mathcal{F}_{\rm DE} \equiv [\det \mathbf{C}(w_0, w_a)]^{-\frac{1}{2}}, \tag{15}$$

where $\mathbf{C}(w_0, w_a)$ is the covariance matrix of the two parameters (Albrecht et al. 2006). Larger values of $\mathcal{F}_{\rm DE}$ represent improved expected measurements, since larger values of $\mathcal{F}_{\rm DE}$ correspond to smaller uncertainties on the two dark energy parameters (w_0, w_a).

Both to generate simulated data set catalogues of type SNeIa that correspond to expected observations at the Rubin Observatory, and then to determine the best-fitting cosmological parameter values and associated uncertainties that result from those catalogues, we use the `CosmoSIS` cosmological parameter estimation code (Zuntz et al. 2015). Approximately 40 000 SNeIa are expected to be observed in at least four filters per year from Rubin (Abell et al. 2009; Ivezić et al. 2019), and thus we generate catalogues of 120 000 SNeIa each, in order to simulate the output of 3 years of Rubin Observatory operation. For the generation of the simulated catalogues, we utilize the same SALT2 parametrization of SNeIa that is used in the joint light-curve analysis (JLA) of 740 observed SNeIa (Betoule et al. 2014). In particular, the generated distributions and correlations of the peak apparent magnitudes in the rest-frame B band $m_B^\star$, the generated observational redshifts z, the light-curve stretch factors X_1, and the colour parameters C of the simulated SNeIa, and the distributions of their respective uncertainties, within the catalogues are generated according to the same distributions and correlations of those observational parameters that are found in the JLA. Both the JLA, and our present analysis, fit the data to a linear model whereby a standardized distance modulus $\mu \equiv 5\log_{10}(d_{\rm L}/10\,{\rm pc})$ is given by

$$\mu = m_B^\star - (M_B - \alpha X_1 + \beta C), \tag{16}$$

where M_B, α, and β are nuisance parameters which respectively correspond to the SNeIa absolute magnitude, and to light-curve stretch and SNeIa colour correction factors to that absolute magnitude. Also similarly to the JLA, and following the procedure previously developed in Conley et al. (2011), we assume that the SNeIa absolute magnitude is related to the host galaxy stellar mass ($M_{\rm stellar}$) by a step function:

$$M_B = \begin{cases} M_B^1 & \text{if } M_{\rm stellar} < 10^{10} M_\odot; \text{ and} \\ M_B^1 + \Delta_M & \text{otherwise.} \end{cases} \tag{17}$$

However, the following modifications are made to the probability density distributions that are used for our catalogue generation:

(i) When generating the simulated SNeIa catalogue that represents expected Rubin observations **with** LPRS-based photometric calibration, the generated systematic uncertainties on the SNeIa magnitudes are reduced by a factor of 2.18 from those in the JLA, corresponding to the expected improvement in SNeIa magnitude measurement from the LPRS-based photometric calibration;

(ii) Also, when generating the simulated SNeIa catalogue that represents expected Rubin observations **with** LPRS-based photometric calibration, the generated systematic covariances between the SNeIa magnitude and light-curve stretch values, as well as between the SNeIa magnitude and colour parameter values, are similarly reduced by a factor of 1.48 from those in the JLA, corresponding to the expected improvement in SNeIa magnitude measurement from LPRS-based photometric calibration.

No modifications to the distributions and correlations of the SALT2 parameters are made when generating the simulated SNeIa catalogue that represents expected Rubin observations **without** LPRS-based photometric calibration. (I.e., the only statistical difference between the observed JLA SNeIa catalogue and the simulated SNeIa catalogue representing expected Rubin observations without LPRS-based photometric calibration is in the size of the catalogue itself: 120 000 SNeIa in the simulated catalogue, vs. 740 SNeIa in the JLA observational catalogue.[15]) The best-fitting central value of w_0 from a combined fit to the JLA data plus complementary probes is -1.018 (Betoule et al. 2014), and thus we set $(w_0, w_a) = (-1.018, 0)$ for the generation of both of our two simulated SNeIa catalogues.

We fit the data within each of the two SNeIa catalogues for Ω_m (the matter density fraction of the critical density) — as well as for the four nuisance parameters α, β, M_B^1, and Δ_M — as free parameters in the fit, which are the same five free parameters as in the nominal JLA data fit. (And as in the nominal JLA data fit, we assume a flat universe: the curvature parameter $\Omega_k = 0$, i.e. the dark energy fraction of the critical density $\Omega_{\rm DE} = 1 - \Omega_m$ in these fits.) However, within these fits to our two simulated catalogues, we also add the w_0 and w_a variables mentioned above as additional free parameters (whereas, in the nominal JLA fit, w_0 is fixed to -1, and w_a is fixed to 0).

The results of the fits to the two simulated catalogues, when projected on to the (w_0, w_a) plane (and, thus, when marginalized over

[15]This is not intended to be a perfect simulation of future Rubin Observatory SNeIa observations. In particular, the redshift distribution of the JLA SNeIa differs from the redshift distribution that is expected from Rubin SNeIa. Another important simplification is the fact the we only generate and fit two simulated catalogues (instead of generating two large sets of simulated catalogues, with each member catalog of each set containing 120 000 SNeIa, then fitting each member catalogue of each set, and then considering the full distributions of the fitted parameter results from each of the two sets of catalogues). However, we note that the present paper is not intended to be centrally focused on SNeIa catalogue simulation and on fits thereof; but rather on the introduction of the concept of an LPRS, and on a simplified estimation of the resulting impact on SNeIa dark energy measurements.

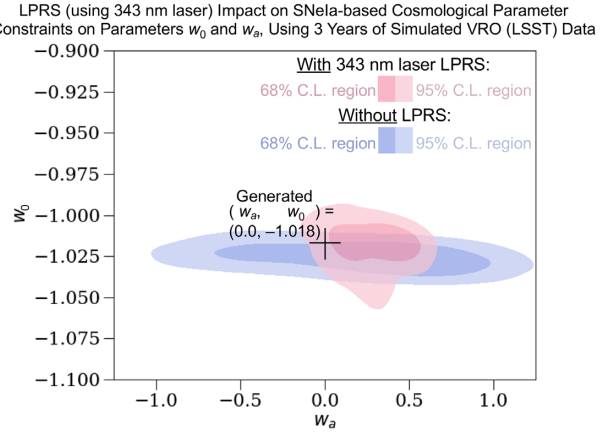

Figure 7. Constraints on the dark energy equation of state parameters w_0 and w_a, obtained using simulated catalogues of type SNeIa. Each one of the two SNeIa catalogues that are fitted to obtain these constraints contains 120 000 simulated SNeIa (corresponding to approximately 3 years of observation at the Rubin Observatory). The generation of the two simulated SNeIa catalogues, as well as the fits that are performed to each catalog, are implemented using the `CosmoSIS` cosmological parameter estimation code (Zuntz et al. 2015), and are explained in the text. The resulting values of the figure of merit parameter $\mathcal{F}_{\rm DE}$ for the fits are 313 for the fit to the SNeIa catalogue representing expected Rubin observations without LPRS-based photometric calibration, and 607 for the fit to the SNeIa catalogue representing expected Rubin observations with LPRS-based photometric calibration. (Also, as would be expected on average, the central values of each fit are approximately one standard deviation away from the generated values of w_0 and w_a.) The fits represent a $\frac{607}{313} = 1.94$-fold expected improvement in the dark energy figure of merit parameter $\mathcal{F}_{\rm DE}$ from LPRS-based photometric calibration (with even greater expected resulting $\mathcal{F}_{\rm DE}$ increases for SNeIa data sets that correspond to greater than 3 years of Rubin Observatory observation).

all of the other fitted parameters listed above), are shown in Fig. 7. The resulting values of the figure of merit parameter $\mathcal{F}_{\rm DE}$ for the fits are 313 for the fit to the SNeIa catalogue representing expected Rubin Observatory observations without LPRS-based photometric calibration, and 607 for the fit to the SNeIa catalogue representing expected Rubin Observatory observations with LPRS-based photometric calibration, representing a $\frac{607}{313} = 1.94$-fold expected improvement in the dark energy figure of merit parameter $\mathcal{F}_{\rm DE}$ from LPRS-based photometric calibration over 3 years of Rubin Observatory observation. (Even larger resulting $\mathcal{F}_{\rm DE}$ increases due to this LPRS-based photometric calibration would be expected for SNeIa data sets that correspond to greater than 3 years of Rubin Observatory observation.)

10 CONCLUSIONS

In summary, we present a method for establishing a precision reference for relative photometry between the visible and NIR (and specifically between photometry at 589 and 819 nm wavelengths) using a powerful, mountaintop-located laser source tuned to the 342.78 nm vacuum excitation wavelength of neutral atoms of sodium. As we have shown, if implemented this method would improve measurements of dark energy from type SNeIa, using upcoming surveys such as the first 3 years of observations at the Vera C. Rubin Observatory, by approximately a factor of 1.94 for the standard dark energy 'figure of merit' $\mathcal{F}_{\rm DE}$ (which is based on the expected uncertainties on measurements of the dark energy equation of state parameters w_0 and w_a).

This method could independently complement and cross-check other techniques under development for photometric calibration, also of unprecedented precision, that utilize laser diode and light-emitting diode light sources carried on a small satellite (Albert 2012) and/or on small high-altitude balloon payloads (Albert et al. 2021b), together with onboard precision-calibrated photodiodes for real-time *in situ* light source output measurement.

The utilization of order-of-magnitude improvement in the precision of relative photometry between the visible and NIR will certainly not be limited only to SNeIa measurements of dark energy. Within other areas of astronomy, precise measurements of stellar populations, photometric redshift surveys, and multiple other astronomical measurements can benefit (Kirk et al. 2015; Connor et al. 2017). Even outside of astronomy, the use of high-precision relative photometry with this technique could potentially help to pinpoint the quantities, types, and movement of aerosols within the Earth's atmosphere above telescopes at night.

This technique could additionally be generalized to other atomic excitations, besides the 342.78 nm excitation of neutral sodium, that also result in fully-mandated cascades consisting of specific ratios of de-excitation photons of different wavelengths.[16] For example (although not so applicable within the atmosphere of Earth), neutral hydrogen atoms have an analogous excitation wavelength of 102.57 nm in vacuum, which would result in a fully-mandated cascade of 656.3 and 121.6 nm photons, which could possibly be used to explore, and to calibrate the exploration of, more H I-rich atmospheres of other planets or moons when using a vacuum-UV laser source tuned to 102.57 nm. Additionally, other neutral alkali metal atoms besides sodium have analogous mandated-cascade-producing excitation wavelengths.

Excitations that result in fully-mandated cascades in the radio and microwave spectra, rather than in the UV, visible, or NIR spectra as in this paper, also almost certainly exist, and thus could most likely be used for high-precision relative radiometry between wavelengths in those spectra, in an analogous manner as with the optical photon technique that we describe. Beyond even photometry and radiometry, the relative polarizations of the emitted de-excitation photons in this technique will be anticorrelated with one another, and thus the precise calibration of relative polarimetry between photons of wavelengths that equal those of the de-excitation photons from a cascade could be performed, especially if the photons emitted from the source laser (or from the source maser) are of a definite and precisely known polarization.

Thus, the technique described in this paper, as well as the related possible techniques mentioned in the above paragraphs in these Conclusions, have prospects not only for SNeIa measurements of dark energy of unprecedented precision; but potentially in addition, more broadly, for other novel measurements that utilize high-precision relative calibration of photometry, radiometry, or polarimetry, both in astronomy and in atmospheric science, across the electromagnetic spectrum.

ACKNOWLEDGEMENTS

The authors would like to thank Prof. Gabriele Ferrari of Università di Trento and of LEOSolutions (Rovereto, Italy) for critical and useful discussions regarding parametric crystal options for laser wavelength tunability; and Dr. Torsten Mans of Amphos GmbH (Aachen, Germany), Dr. Knut Michel of TRUMPF GmbH (Ditzingen, Germany), and Dr. Jochen Speiser of the German Aerospace Center Institute

[16] In analogy with LIDAR, the generalized technique could perhaps be termed LIght Detection And Spectro-Photometry.

of Technical Physics (Stuttgart, Germany) for further critical and useful discussions regarding single-mode Yb:YAG disc pump lasers. We would also like to thank Prof. Chris Pritchet of the University of Victoria for reading over the manuscript and providing extremely helpful comments and suggestions. JEA gratefully acknowledges support from Canadian Space Agency grants 19FAVICA28 and 17CCPVIC19.

DATA AVAILABILITY

All code and data generated and used for the results of this paper is available from the authors upon request.

REFERENCES

Abell P. A. et al., 2009, preprint (arXiv:0912.0201)
Aghanim N. et al., 2020, A&A, 641, A6
Albert J. E., 2012, AJ, 143, 8 [17]
Albert J. E., Budker D., Chance K., Gordon I. E., Bustos F. P., Pospelov M., Rochester S. M., Sadeghpour H. R., 2021a, MNRAS, 505, 48XX (Paper II)
Albert J. E., Brown Y. J., Stubbs C. W., 2021b, in preparation (please see http://projectaltair.org)
Albrecht A. et al., 2006, preprint (arXiv:astro-ph/0609591)
Ali M. A., 1971, J. Quant. Spectrosc. Radiat. Transf., 11, 1611
Antcheva I. et al., 2011, Comput. Phys. Commun., 182, 1384 (see also https://root.cern.ch)
Baumgardner J. et al., 2021, J. Geophys. Res. Planets, 126, e2020JE006671
Betoule M. et al., 2014, A&A, 568, A22
Bohlin R. C., Gilliland R. L., 2004, AJ, 127, 3508
Bonaccini D. et al., 2002, Proc. SPIE Vol. 4494, Adaptive Optics Systems and Technology II, 4494, 276
Brun R., Rademakers F., 1997, Nucl. Instrum. Methods Phys. Res., 389, 81 (see also https://root.cern.ch)
Buldakov M. A. et al., 1996, Spectrochim. Acta A, 52, 995
Calia D. B., Hackenberg W., Holzlöhner R., Lewis S., Pfrommer T., 2014, Adv. Opt. Technol., 3, 345
Cerny T., Sechrist C. F., 1980, Technical report (see https://core.ac.uk/download/pdf/42859374.pdf), Aeron. Rep. No. 94. Aeron. Lab. Univ. of Illinois, Urbana, IL
Chapman S., 1939, ApJ, 90, 309
Chen M. et al., 2016, J. Lumin., 172, 254
Conley A. et al., 2011, ApJS, 192, 1
Connor T. et al., 2017, ApJ, 848, 37
Doi M. et al., 2010, AJ, 139, 1628
Fan T., Zhou T., Feng Y., 2016, Sci. Rep., 6, 19859
Foy R., Pique J.-P., 2004, in Webb C. E., Jones J. D. C., eds, Lasers in Astronomy, Vol. 1, Handbook of Laser Technology and Applications. Institute of Physics, London, p. 2581
Foy R. et al., 1995, A&AS, 111, 569
Foy R. et al., 2000, J. Opt. Soc. Am. A, 17, 2236
Gordon I. E. et al., 2017, J. Quant. Spectrosc. Radiat. Transf., 203, 3
Hertel I. V., Ross K. J., 1969, J. Phys. B, 2, 285
Holberg J. B., Bergeron P., 2006, ApJ, 132, 1221
Holzlöhner R. et al., 2010, Proc. SPIE, 7736, 77360V
IPG Photonics Inc. (Oxford, MA, USA), 2021, product no. VLR-532-1000. Available at: https://www.ipgphotonics.com/en/196/FileAttachment/VLM-VLR-532+Datasheet.pdf and product no. YLR-1030-1000, https://www.ipgphotonics.com/en/167/FileAttachment/YLR-1030+Series+Datasheet.pdf
Ivezić Ž. et al., 2019, ApJ, 873, 111
Jones D. O. et al., 2018, ApJ, 857, 51
Jones L., 2017, Technical report, Calculating LSST Limiting Magnitudes and SNR. LSST/VRO Simulation Technical Note 002 (SMTN-002) (https://smtn-002.lsst.io)
Jones L. et al., 2019, Systems Engineering-approved LSST Throughputs Repository. Available at: https://github.com/lsst-pst/syseng_throughputs
Juncar P., Pinard J., Harmon J., Chartier A., 1981, Metrologia, 17, 77
Kane T. J., Hillman P. D., Denman C. A., 2014, SPIE Conf. Ser. Vol. 9148, Adaptive Optics Systems IV, 9148, 91483G
Kelleher D. E., Podobedova L. I., 2008, J. Phys. Chem. Ref. Data, 37, 267
Kirk D. et al., 2015, MNRAS, 451, 4424
Kramida A. et al., 2020, Technical report, Atomic Spectra Database (ver. 5.8). NIST. Available at: https://physics.nist.gov/asd
Lahav O., Liddle A. R., 2019, Prog. Theor. Exp. Phys., 2020, 083C01
Linder E. V., 2003, Phys. Rev. Lett., 90, 091301
McEachran R. P., Cohen M., 1973, J. Quant. Spectrosc. Radiat. Transf., 13, 197
Mégie G., Bos F., Blamont J. E., Chanin M. L., 1978, Planet. Space Sci., 26, 27
Meißner K. W., Luft K. F., 1937, Ann. Phys. (Leipzig), 421, 698
Moldovan I. C., Fesquet V., Marc F., Guillet de Chattelus H., Pique J.-P., 2007, Ann. Phys. Fr., 32, 91
Moussaoui N. et al., 2010, A&A, 511, A31
Olivier S. S., Max C. E., 1994, in Robertson J. G., Tango W. J., eds, IAU Symp. 158, Laser Guide Star Adaptive Optics: Present and Future. Kluwer, Dordrecht, p. 283
Pedreros Bustos F. et al., 2018, Nat. Commun., 9, 3981
Pedreros Bustos F. et al., 2020, J. Opt. Soc. Am. B, 37, 1208
Perlmutter S. et al., 1999, ApJ, 517, 565
Pique J.-P., Moldovan I. C., Fesquet V., 2006, J. Opt. Soc. Am. A, 23, 2817
Plane J. M. C., Feng W., Dawkins E. C. M., 2015, Chem. Rev., 115, 4497
Potter A. E., Morgan T. H., 1988a, Geophys. Res. Lett., 15, 1515
Potter A. E., Morgan T. H., 1988b, Science, 241, 675
Riess A. G. et al., 1998, AJ, 116, 1009
Simbotin I., Marinescu M., Sadeghpour H. R., Dalgarno A., 1997, J. Chem. Phys., 107, 7057
Slipher V. M., 1929, PA, 37, 328
Stubbs C. W., Tonry J. L., 2006, ApJ, 646, 1436
Stubbs C. W. et al., 2010, ApJS, 191, 376
Tatarski V. I., 1961, Wave Propagation in a Turbulent Medium. McGraw-Hill, New York (ISBN 978-0486810294)
Thorlabs Inc. (Newton, NJ, USA), 2021, product no. FELH0500. Available at: https://www.thorlabs.com/newgrouppage9.cfm?objectgroup_id=6082&pn=FELH0500 and optical coating K07, https://www.thorlabs.com/newgrouppage9.cfm?objectgroup_id=806
TRUMPF GmbH (Ditzingen, Germany), 2021, TruDisk product line. Available at: https://www.trumpf.com/en_CA/products/lasers/disk-lasers/trudisk/product_data_sheet/download/TruDisk.pdf and TruDisk with green wavelength, https://www.trumpf.com/en_CA/products/lasers/disk-lasers/trudisk-with-green-wavelength/product_data_sheet/download/TruDisk%2520with%2520green%2520wavelength.pdf
Tyson R. H., 2015, Principles of Adaptive Optics, 4th edn. CRC Press, Boca Raton (ISBN 978-1439808580)
Vogt F. P. A., 2019, Phys. Rev. Lett., 123, 061101
Vogt F. P. A. et al., 2017, Phys. Rev. X, 7, 021044
Weinberg S., 1989, Rev. Mod. Phys., 61, 1
Wizinowich P. L. et al., 2006, PASP, 118, 297
Wood-Vasey W. M. et al., 2007, ApJ, 666, 694
Zuntz J. et al., 2015, Astron. Comput., 12, 45 (with code repository and instructions available at https://bitbucket.org/joezuntz/cosmosis/wiki/Home)

[17]Please additionally see https://www.orcasat.ca (ORCASat Collaboration), 2021.

This paper has been typeset from a TEX/LATEX file prepared by the author.